IOPscience iopscience.iop.org

Home Search Collections Journals About Contact us My IOPscience

Design and characterization of a 3D MEMS VOA driven by hybrid electromagnetic and electrothermal actuation mechanisms

This article has been downloaded from IOPscience. Please scroll down to see the full text article.

2012 J. Micromech. Microeng. 22 105031

(http://iopscience.iop.org/0960-1317/22/10/105031)

View the table of contents for this issue, or go to the journal homepage for more

Download details:
IP Address: 137.132.3.10
The article was downloaded on 11/09/2012 at 03:34

Please note that terms and conditions apply.

IOP Publishing | Journal of Micromechanics and Microengineering

J. Micromech. Microeng. **22** (2012) 105031 (13pp) doi:10.1088/0960-1317/22/10/105031

Design and characterization of a 3D MEMS VOA driven by hybrid electromagnetic and electrothermal actuation mechanisms

Kah How Koh, You Qian and Chengkuo Lee[1]

Department of Electrical & Computer Engineering, National University of Singapore, 4 Engineering Drive 3, Singapore 117576

E-mail: elelc@nus.edu.sg

Received 14 March 2012, in final form 11 June 2012
Published 10 September 2012
Online at stacks.iop.org/JMM/22/105031

Abstract
By using a CMOS compatible process technology, a MEMS variable optical attenuator (VOA) is characterized in terms of actuation mechanisms. A dual-fiber collimator is aligned perpendicularly to the micromirror in a three-dimensional (3D) free space configuration, where the micromirror is mechanically connected with an electromagnetic actuator and two sets of electrothermal actuators. Three types of attenuation schemes based on electromagnetic, electrothermal and hybrid, i.e. combination of electrothermal and electromagnetic, actuations have been explored and studied. Dynamic attenuation ranges of 40 dB have been achieved at 4 V_{dc}, 26 mW and 3 $V_{dc,}$ 20 mW by electromagnetic and electrothermal attenuation schemes respectively. Wavelength-dependent loss has been demonstrated to be less than 0.6 dB at all attenuation states for both attenuation schemes. In the hybrid attenuation scheme, various voltage combinations are made to the electromagnetic and electrothermal actuators. An optical attenuation of approximately 40 dB can be obtained when two volts are applied to both the electromagnetic and electrothermal actuators simultaneously, while the electrical power consumption of the actuators is 17 mW in total. Our unique design of using both electrothermal and electromagnetic actuators simultaneously to achieve attenuation is the first demonstration of such a hybrid-driven CMOS compatible MEMS VOA device.

(Some figures may appear in colour only in the online journal)

1. Introduction

Micro-opto-electro-mechanical systems (MOEMS) technology has been a promising candidate for a wide variety of applications such as microscanners [1–5], optical coherence tomography [6–7] and microspectrometry [8]. In the late 1990s and early 2000, significant progress in the MOEMS technology, alongside with the development of dense wavelength division multiplexing (DWDM) systems, has been made in the telecommunication industry. Enormous investment has been made in MOEMS technology as it has been recognized to be an indispensable tool needed to fulfill the missing link that can help connect other existing technologies to form an all-optical communication network [9–12]. Many crucial MEMS-based components such as variable optical attenuators (VOAs) [13], optical switches [14–16] and tunable lasers [17] have been deployed in various modules of the fiber-optic communication network. MEMS VOAs have been one of the most attractive devices in the optical communication market due to their widespread presence in the wavelength multiplexing (MUX) and demultiplexing (DMUX) nodes of the DWDM system.

Prior to the discussion of the various MEMS VOA devices reported in the literature, it is worthwhile recalling the different kinds of mainstream actuation mechanisms that are commonly used in the field of MOEMS [18]. These mechanisms include piezoelectric, electrostatic,

[1] Author to whom any correspondence should be addressed.

 © 2012 IOP Publishing Ltd Printed in the UK & the USA

electromagnetic and electrothermal. Piezoelectric-driven micromirrors have highly repeatable results with low actuation voltage as piezoelectric material, such as $PbZrTiO_3$ (PZT), has the highest energy density compared to other silicon-based actuators [19–21]. However, limited material selection in CMOS manufacturing line and CMOS compatible processes restricted the actuators to be mainly that of electrostatic, electrothermal and electromagnetic [22–24]. Electrostatic comb-drive micromirrors have also been reported and despite being a versatile and simple actuation mechanism, there is low force generation, hence requiring a high biasing voltage [25–26]. In addition, there is an electrostatic instability due to the pull in voltage and the optical behavior is largely nonlinear. In contrast, electrothermal bimorph actuators provide large stroke force and static mechanical deflection angle to the mirror plate at a relatively low driving voltage [27–29]. Unfortunately, electrothermal actuators do have some inherent limitations such as large power consumption, slow response and their optical behavior dependence on ambient temperature. Similarly, electromagnetic actuated mirrors can achieve a large mechanical rotation angle, but they require bulky external magnet cores for actuation, making compact packaging challenging [30, 31].

Utilizing the various actuation mechanisms described above, several research groups have successfully demonstrated MEMS VOAs based on different actuation and attenuation configurations. The first MEMS-based VOAs were developed in 1998 by two groups from Lucent Technology [32] and another group led by Professor de Rooij at University of Neuchâtel, Switzerland [33]. In both designs, surface-micromachined poly-Si shutters driven by the electrostatic force are arranged between the coaxially aligned input and output fibers and attenuation was achieved by actuating the shutter and tuning the percentage of light blocked by the shutters. Another surface micromachined in-plane MEMS VOA using an electrostatic-driven pop-up microshutter fixed on a drawbridge plate had also been reported by Liu *et al* [34]. The device demonstrated 1.5 dB insertion loss and 45 dB attenuation under 8 V_{dc}, with the driving voltage reduced substantially through the use of this unique drawbridge structure.

Besides shutter-type MEMS VOAs [32–39], there are also two more groups of MEMS VOAs reported in the literature; planar reflective and three-dimensional (3D) reflective. In planar reflective-type MEMS VOAs, two commonly adopted designs include using single reflective [40–42] and retro-reflective mirrors [43–46]. With proper design of actuators, a well-optimized DRIE process and appropriate selection of lens fibers, single-reflective-type VOAs performance are superior to shutter-type VOAs. Combining optics and a tilt mirror to be assembled in a 3D configuration is also another key approach to make MEMS VOA devices [47–49]. When tilt mirrors are deployed for 3D VOA in conjunction with large micro-optics such as a dual-fiber collimator, the resulting VOA device can gain excellent data in terms of return loss, polarization-dependent loss and wavelength-dependent loss under a reasonable driving voltage and small rotational angle. Isamoto *et al* have demonstrated a 3D VOA using the electrostatic parallel plate actuator in which the derived performance was outstanding as only 4.5 V_{dc} was needed to achieve 0.3° rotational angle and 40 dB attenuation range [47]. Recently, we have also developed two 3D MEMS VOA devices based on piezoelectric actuation, where these works are the first reported attempt of 3D attenuated MEMS VOAs using crystalline PZT thin film actuators [48, 49]. Both of our designs were based on piezoelectric actuation and required only 1 V_{dc} to achieve 40 dB dynamic range of attenuation.

From the literature review above, it can be observed that limited research effort has been reported in 3D MEMS VOAs in contrast to the widely reported activities in planar MEMS VOAs. Although 3D MEMS VOAs driven by piezoelectric PZT actuators have been demonstrated to achieve 40 dB at 1 V_{dc} previously [48, 49], PZT is not a CMOS compatible material. With the future vision of having a monolithic integrated MEMS VOA with CMOS-integrated circuits, we endeavor to develop a novel and CMOS compatible actuation mechanism to achieve optical attenuation. Thus, in this paper, we explore a new 3D MEMS VOA that can be operated in either electrothermal or electromagnetic attenuation schemes. In addition, by addressing voltage biases to both the electrothermal and electromagnetic actuators simultaneously, i.e. hybrid attenuation scheme, we can obtain better performance in terms of reduced electrical power consumption and obtaining an additional degree of freedom in attenuation control. Our approach of using the hybrid attenuation scheme differs greatly from all of the planar and 3D MEMS VOA designs that have already been reported in the literature where only one type of actuation mechanism is used to drive the mirror/shutter in order to achieve attenuation. The attenuation efficiency for electromagnetic, electrothermal and hybrid attenuation schemes will be studied in detail in this research attempt. As such, our unique design of using both electrothermal and electromagnetic actuators to achieve attenuation is the first demonstration of such a hybrid-driven CMOS-compatible MEMS VOA device.

2. Design and modeling

A schematic diagram of the proposed hybrid 3D MEMS VOA is shown in figure 1. There are four sets of electrothermal actuators along the longitudinal sides of the mirror which are responsible for the rotation of the mirror plate about the *x*-axis. The electrothermal actuators are anchored to the substrate and joined to the frame by the thick and rigid C-shaped joints. The frame is embedded with numerous turns of aluminum (Al) electromagnetic coils, during which a Lorentz force and rotation of the mirror about *z*-axis will be generated when a current flows in the coils in the presence of a permanent magnetic field. The mirror surface is deposited with Al and is connected to the frame by the T-shaped torsion bars. The dual fiber collimator is arranged in a 3D free-space configuration where the infrared (IR) laser beam focuses on the center of the Al mirror surface. With both rotation axes being orthogonal to each other, the micromirror is able to move with six degrees of freedom for enabling the 3D attenuation scheme. Insets (*A*) and (*B*) in figure 1 show the top view drawing illustrating

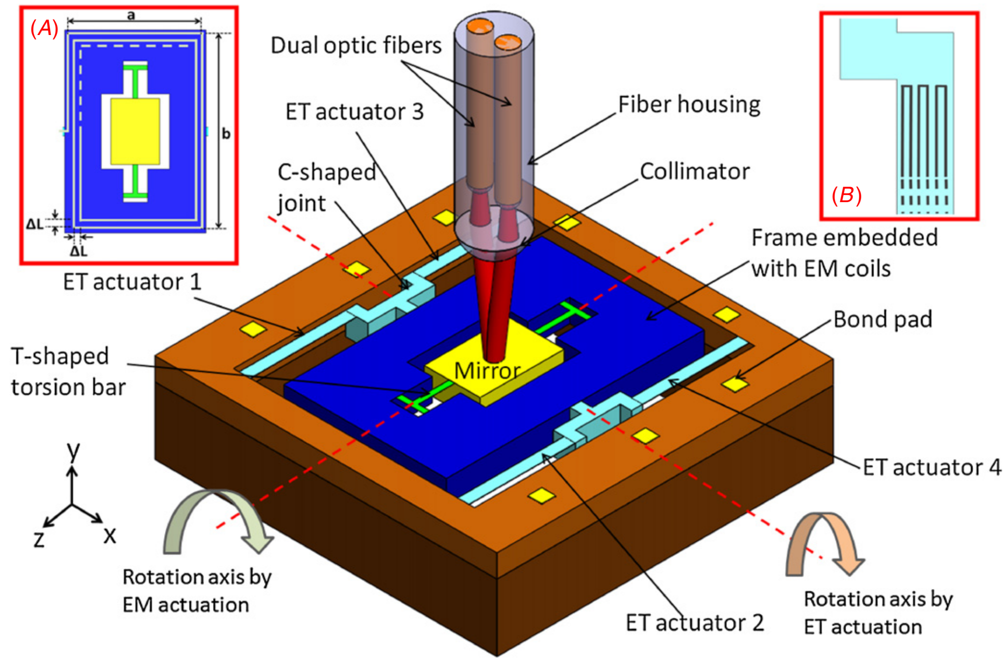

Figure 1. Schematic diagram of the hybrid-actuated MEMS VOA with dual-fiber collimator arranged in 3D free space configuration such that the light beam focuses on the center of the aluminum mirror surface. Insets (*A*) and (*B*) show the top view drawings illustrating the dimensions and layout of the EM coils and ET windings respectively. The number of EM coils and ET windings have been reduced for simplicity purposes.

the dimensions and layouts of the electromagnetic coils and electrothermal windings respectively. The numbers of turns of electromagnetic coils and electrothermal windings shown in the insets have been reduced for simplicity purposes. The details of the attenuation principle by the two modes of actuation, i.e. electromagnetic and electrothermal, will ensue on in this section.

2.1. Electromagnetic actuation and attenuation principle

Figure 2(*a*) shows the schematic diagram of the electromagnetic actuation mechanism in the presence of an external magnetic field and current flowing in the electromagnetic coils. Two layers of electromagnetic coils, made of Al, are deposited and patterned on the silicon (Si) frame. A pair of magnets may be arranged such that a uniform permanent magnetic field in the *x*-direction may be formed across the device. When the electromagnetic coils are biased and a current flows in an anticlockwise direction as shown in figure 2(*a*), a pair of equal but opposite Lorentz force will be generated at the coils orthogonal to the magnetic field, i.e. those coils running along the *z*-direction. The out-of-plane Lorentz force acting on a dc carrying conductor is given as

$$F = \oint_L I\,\mathrm{d}l \times B \tag{1}$$

where *I* is the current flowing in a closed loop conductor of length *L* and *B* is the external permanent magnetic field. This pair of Lorentz forces introduces a magnetic torque and causes the mirror to rotate about the *z*-axis. The torque generated may be approximated as

$$T = 2iB \sum_{m=0}^{N-1} (b - 2m \bullet \Delta l)\,(a - 2m \bullet \Delta l) \tag{2}$$

where *i* is the current flowing in the electromagnetic coils, *B* is the magnetic field strength of the magnet (0.15 *T*), *N* is the number of coil turns in each layer (54) *a* and *b* are the side lengths of the most outer coil turn on the short (2.83 mm) and long sides (4.55 mm) of the frame respectively, ΔL is the pitch of the electromagnetic coils (12 μm) as shown in the inset of figure 1. Thus, from (2), it can be deduced that a greater mechanical rotation angle of the mirror is obtained when a larger current, stronger magnet and greater number of coil turns are fabricated on the device.

Figure 2(*b*) shows the schematic diagram illustrating the electromagnetic attenuation principle, where the laser beam is rotated and displaced by an angle θ_{EM} and distance $\delta_{\mathrm{EM,laser}}$ respectively. When there is no current flowing in the electromagnetic coils, the normal of the mirror surface is perfectly aligned with the IR laser beam, causing all the light to be coupled from the input fiber to the output fiber. When the mirror rotates about the *z*-axis due to the magnetic torque acting on the frame, the reflected laser beam is rotated and displaced by an angle θ_{EM} and distance $\delta_{\mathrm{EM,laser}}$ respectively. A portion of the laser beam no longer couples into the output fiber, resulting in attenuation. An analytical model relating the optical scan angle (θ_{EM}) to the displacement of the reflected laser beam from its original position can be derived from figure 2(*b*) and is represented by (3) and (4):

$$\theta = \tan^{-1}\left(\frac{A}{\mathrm{WD}}\right) \tag{3}$$

$$\delta_{\mathrm{EM,laser}} = D * \tan\left(\theta + \theta_{\mathrm{EM}}\right) - A \tag{4}$$

where θ_{EM} is the optical scan angle of the laser beam when the electromagnetic coils are dc biased, *A* is the

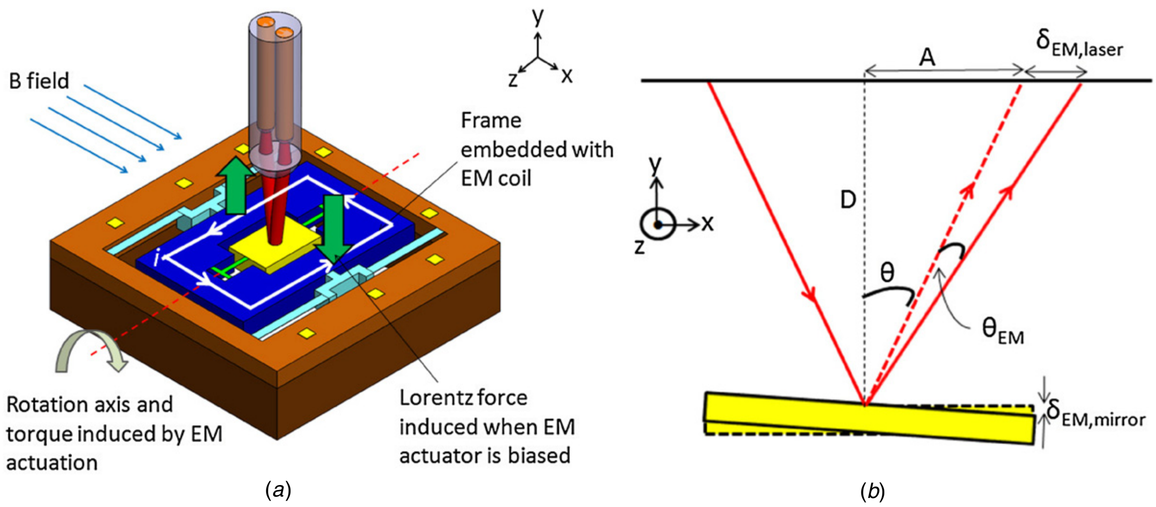

Figure 2. Schematic diagram showing the (*a*) EM actuation mechanism in the presence of an external permanent magnetic field and current flowing in the coils embedded in the frame; (*b*) EM attenuation principle, where the laser beam is rotated and displaced by an angle θ_{EM} and distance $\delta_{EM,laser}$ respectively.

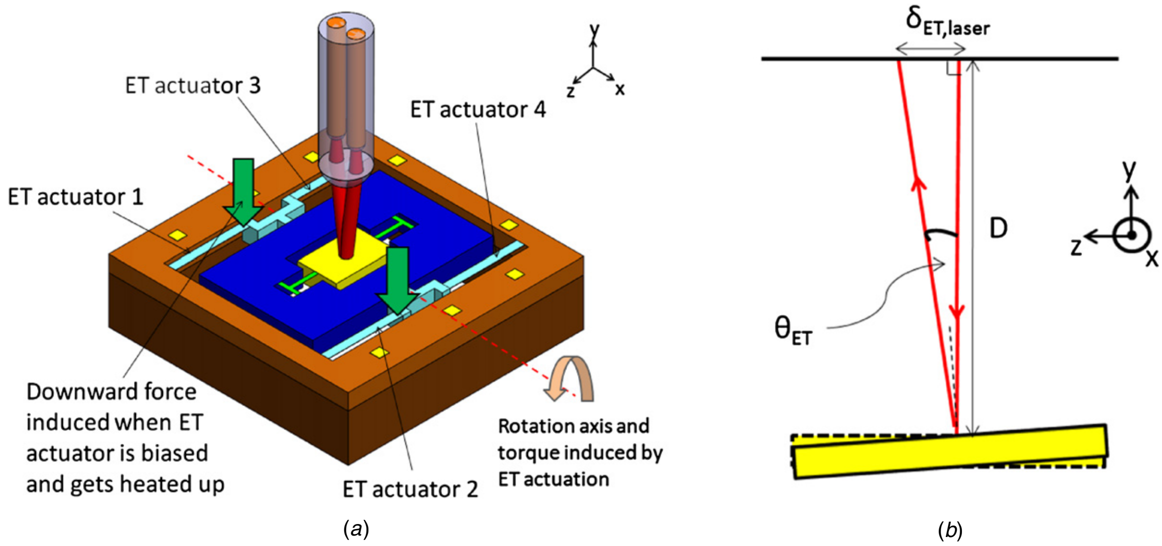

Figure 3. Schematic diagram showing the (*a*) ET actuation mechanism where ET actuators 3 and 4 are biased and heated up; (*b*) ET attenuation principle, where the laser beam is rotated and displaced by an angle θ_{ET} and distance $\delta_{ET,laser}$ respectively.

half distance between the input and output fiber in the dual-fiber collimator (100 μm), D is the working distance (1 mm), θ is the angle between the incident laser beam and normal of the mirror before actuation, $\delta_{EM,laser}$ is the displacement of the reflected laser from its original position during electromagnetic actuation. With the above-mentioned equations (3) and (4), the theoretical displacement of the laser beam from its original position ($\delta_{EM,laser}$) can be calculated using the experimental optical scan angle data (θ_{EM}) obtained by impinging a red visible laser light on the mirror surface.

2.2. *Electrothermal actuation and attenuation principle*

Figure 3(*a*) shows the schematic diagram of the electrothermal actuation mechanism when electrothermal actuators 1 and 2 are biased. The electrothermal actuator consists of a Si cantilever made from the device layer of a silicon-on-insulator (SOI) wafer and Al heater deposited and patterned on it. As shown in inset B of figure 1, the Al heater is patterned in a winding manner so as to increase the resistance and thermal reliability of the heater and actuator respectively. There are a total of 14 electrothermal windings fabricated on each of the four actuators. A thin layer of silicon dioxide (SiO_2), which acts as thermal insulation, is deposited around the Al heater. When a current flows through the windings, the Al heats up and expands more than Si, causing the electrothermal actuator to bend downward. To introduce a mechanical torque about the *x*-axis, both actuators 1 and 2 or 3 and 4 are to be biased serially so that either set of actuators experiences downward displacements simultaneously. As shown in figure 3(*b*), when the mirror undergoes rotation about the *x*-axis, the reflected IR laser beam is displaced by an angle θ_{ET} and distance $\delta_{ET,\,laser}$ respectively. A portion of the laser beam no longer couples into the output fiber, resulting in attenuation. A similar analytical model relating the optical scan angle (θ_{ET})

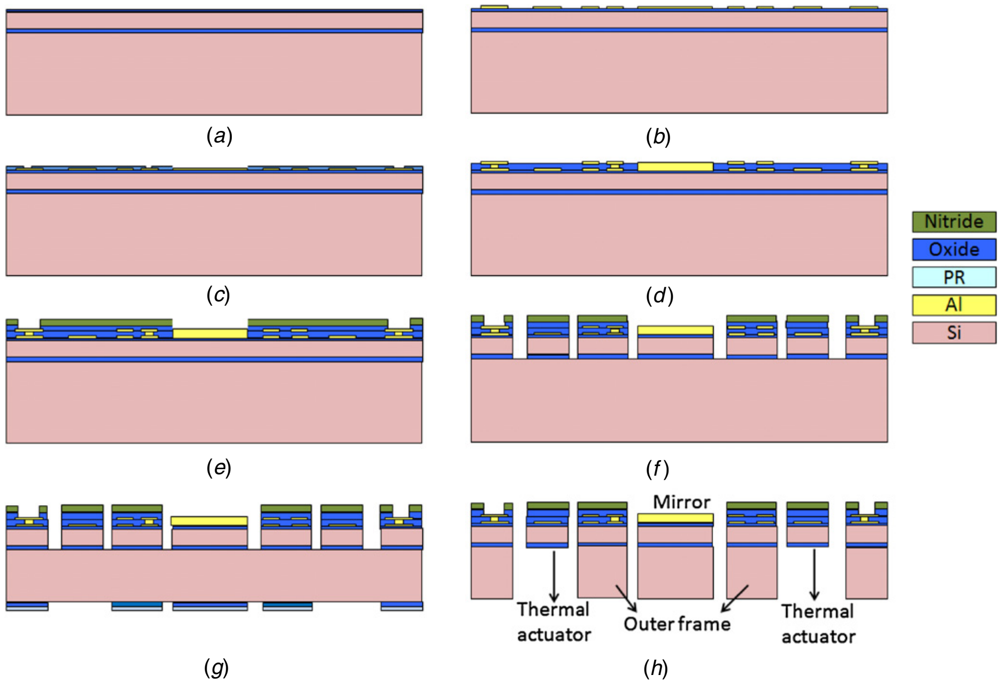

Figure 4. CMOS-compatible microfabrication process flow for the hybrid-actuated MEMS VOA. (*a*) Deposition of SiO_2 on the SOI wafer. (*b*) Deposition and patterning of first Al layer. (*c*) Deposition of SiO_2 followed by bond pad opening. (*d*) Deposition and patterning of second Al layer. (*e*) Deposition of SiO_2 and Si_3N_4 followed by contact-hole opening. (*f*) Frontside release of device. (*g*) Grinding of wafer followed by backside deposition and patterning of SiO_2. (*h*) Backside DRIE to release microstructures.

to the displacement of the reflected laser beam from its original position ($\delta_{ET,\ laser}$) can be made from figure 3(*b*) and is represented by (5)

$$\delta_{ET,laser} = D * \tan(\theta_{ET}) \quad (5)$$

where θ_{ET} is the optical scan angle of the laser beam when the electrothermal actuators 3 and 4 are dc biased, D is the working distance (1 mm), $\delta_{ET,laser}$ is the displacement of reflected laser from its original position during electrothermal actuation. With equation (5), the theoretical displacement of the laser beam from its original position can also be calculated using the experimental optical scan angle data obtained during electrothermal actuation.

3. Microfabrication and experimental setup

Figure 4 shows the CMOS-compatible microfabrication process flow for the hybrid-actuated MEMS VOA. A SOI wafer with a 3 μm thick Si device layer is first deposited with a 0.2 μm thick insulating plasma enhanced chemical vapor deposited (PECVD) silicon dioxide (SiO_2) as shown in figure 4(*a*). In figure 4(*b*), a 2 μm thick Al is physical vapor deposited (PVD) and patterned to form the electrothermal windings, electromagnetic coils, bond pads and mirror surface. This is followed by deposition of 0.5 μm thick PECVD SiO_2 in figure 4(*c*), where the SiO_2 serves as thermal and electrical insulation for the electrothermal windings and electromagnetic coils respectively. Similar to figure 4(*b*), a second layer of PVD Al, with exception to the electrothermal windings, is again deposited, patterned and etched in figure 4(*d*). In figure 4(*e*), silicon dioxide and nitride, each of 0.5 μm thickness, are deposited as passivation layers. This is followed by reactive ion etching (RIE) of the silicon dioxide and nitride layers for contact-hole opening. Al remains as the top layer in the mirror region so as to enhance the reflectivity of IR light impinged on the mirror surface. The microstructures such as the electrothermal actuators, C-shaped joints, T-shaped torsion bars and micromirror are then defined from the frontside in figure 4(*f*) through RIE of silicon nitride, SiO_2, Si device and buried oxide (BOX) layers using CF_4 (for silicon nitride), CHF_3 (for SiO_2 and BOX) and SF_6 (for Si) respectively.

After all the frontside wafer processes are finished, the Si handle layer is reduced to 450 μm through backside grinding and polishing as shown in figure 4(*g*). This is followed by backside deposition and patterning of 2 μm thick PECVD SiO_2. The photoresist that is used to pattern the SiO_2 layer remains behind at the backside of the wafer so that both the photoresist and the SiO_2 can function as hard mask materials for the Si DRIE during the subsequent step. The DRIE process in figure 4(*h*) is conducted in a time-controlled manner as the process does not stop effectively on the 1.1 μm thick BOX layer. A coarse DRIE step is first performed by removing approximately 400 μm thick handle layer. This is followed by several fine DRIE steps of 5 min each so as to gradually remove the remaining 50 μm of the silicon handle layer. The wafer is taken out after each etch step and the backside of the wafer is checked under the optical microscope so as to determine whether the entire Si handle layer has been fully etched away. Figure 5 shows the fabricated MEMS VOA device of size 6 mm $\times$ 6 mm, wire-bonded to a dual inline package (DIP). The rectangular mirror is 1.5 mm $\times$ 1 mm in size, with its surface deposited with 4 μm thick Al. Insets (*A*) and (*B*) show

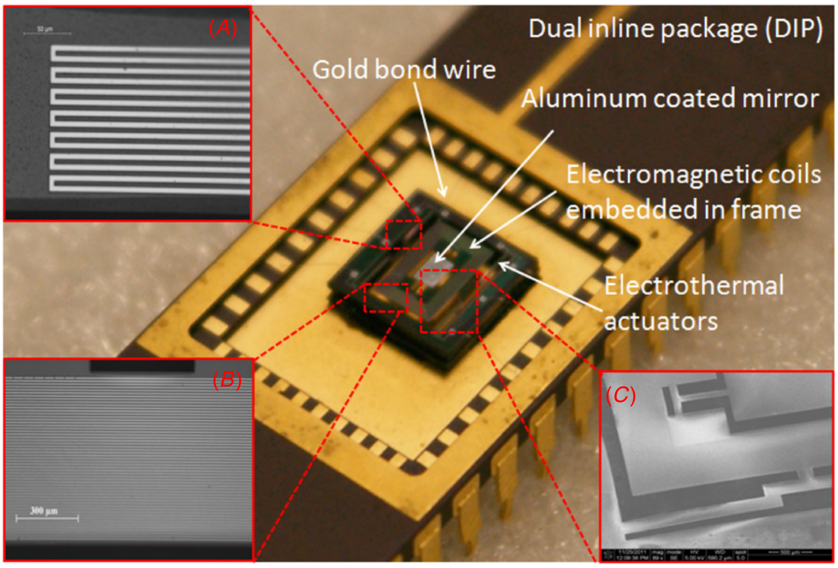

Figure 5. A magnified photo showing the packaged MEMS VOA device. Insets (*A*) and (*B*) show the optical micrographs of the ET windings and EM coils respectively. Inset (*C*) shows a SEM micrograph of the ET actuator, C-shaped joint, frame, T-shaped torsion bar and mirror.

Table 1. Detailed dimensions of the microstructures in the MEMS VOA device.

Structural parameters	Values
Size of the die	6 mm $\times$ 6 mm
Mirror (l $\times$ w $\times$ t)	1.5 mm $\times$ 1 mm $\times$ 0.45 mm
T-shaped torsion bar (w $\times$ t)	150 μm $\times$ 5 μm
Electrothermal actuator (l $\times$ w $\times$ t)	1850 μm $\times$ 200 μm $\times$ 7 μm
Electrothermal actuator winding (l $\times$ w $\times$ t)	1800 μm $\times$ 5 μm $\times$ 2 μm
No. of windings for electrothermal actuator	14
Electromagnetic coil (w $\times$ t)	3 μm $\times$ 2 μm
Total no. of electromagnetic coils	108

the optical micrographs of the windings on the electrothermal actuator and electromagnetic coils on the frame respectively. Each electrothermal actuator has 14 Al windings of width 5 μm, while a total of 108 turns, each of width 3 μm, are fabricated in the two layers of electromagnetic coils. Inset (*C*) shows a SEM micrograph of the device, which includes the electrothermal actuator, C-shaped joint, frame, T-shaped torsion bar and micromirror. The detailed dimensions of the microstructures in the MEMS VOA device are summarized in table 1.

The schematic diagram of the measurement setup for MEMS VOA characterization is illustrated in figure 6(*a*). The optical measurement setup consists of a tunable IR laser source integrated with a power meter (Agilent 8164B Lightwave Measurement System), two multiaxis X–Y–Z–θx–θz adjustable stages, dual fiber with collimator and two dc power supplies. The device is mounted on the first adjustable stage via the breadboard while the dual fiber with collimator is mounted on the second adjustable stage via a fiber holder. The dual-fiber collimator is placed at a working distance of 1 mm away from the mirror surface. The input IR light from the tunable laser is launched via one fiber, i.e. input fiber of the dual fiber through the collimator to the center of the mirror. The reflected light is collected by the same collimator to the power meter via the output fiber of the dual fiber. Two dc power supplies are used so that the electrothermal actuators and the electromagnetic coils can be biased separately. The power of the IR laser source used in the experiment is 4 mW. The collimated beam diameter has been characterized to be 700 μm $\pm$ 25 μm, which is smaller than the mirror. The whole measurement setup is established on an antivibration optical table to reduce the effect of ambient shock to the characterization setup. Figure 6(*b*) illustrates a photo of the actual measurement setup on an optical table while figure 6(*c*) shows a magnified photo of the device under test (DUT) region, where the DUT is mounted upright in the presence of a permanent magnetic field generated by a pair of Alcomax III magnets. The magnetic field strength at the center of the magnetic field is measured by a Gauss meter to be approximately 0.15 T.

For the initial insertion loss measurement, the relative position of the collimator and mirror is adjusted such that the coupling loss is optimized or minimized. In order to do so, red laser light of 632.8 nm is first shone through the collimator onto the center of the mirror. Both the stages are adjusted so that the red laser spot is centralized at the middle of the mirror. The IR tunable laser source is then fed into the input fiber after the coarse alignment step has been confirmed. During the fine alignment step, the relative position of the mirror to the collimator is adjusted by moving and tilting both X–Y–Z–θx–θz stages such that minimum insertion loss is obtained. The θx and θz adjustment knobs enable the stage to be tilted with regard to the x- and z-axis respectively. The measured insertion loss in this setup is about 1.8 dB, which is about a decibel higher than commercial VOA products. This is mainly caused by the surface warpage of the mirror and

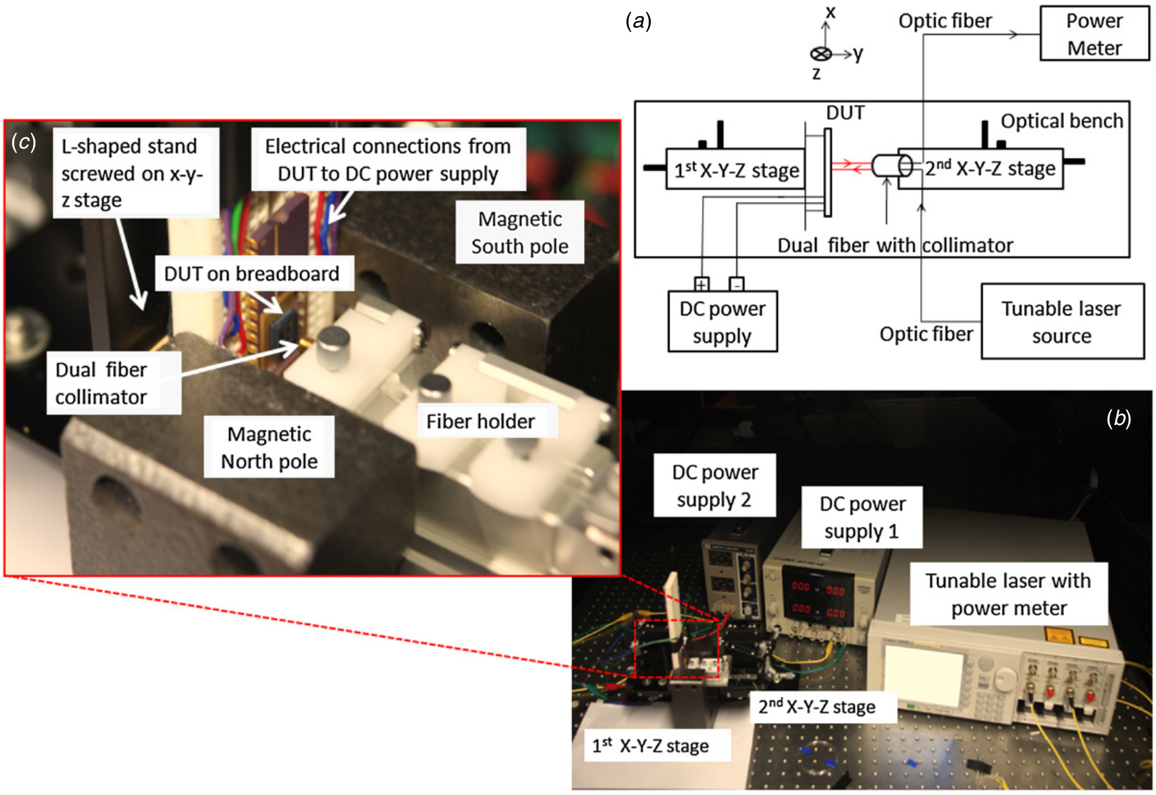

Figure 6. (*a*) Schematic diagram of the measurement setup carried out on an antivibration optical bench. The stages are capable of moving in *X*–*Y*–*Z* directions and tilting along *X*–*Y* (θz) and *Y*–*Z* (θx) planes as well. (*b*) Photograph illustrating the actual measurement setup which includes the tunable laser integrated with a power meter, two dc power supplies and stages. (*c*) A magnified photograph at the DUT region, where the DUT is mounted upright in the presence of an external permanent magnetic field. The dual-fiber collimator is adjusted to a working distance of 1 mm away from the mirror surface.

the inferior reflectivity of the Al coating compared to gold at 1550 nm. Further optimization of the VOA fabrication may reduce the insertion loss to less than 1 dB.

4. Results and discussion

The *I*–*V* curves of the electromagnetic coils and electrothermal actuators are obtained from an Agilent b1500a Semiconductor Device Analyzer and shown in figure 7. A current of 6.6 mA is obtained when 4 V_{dc} is applied to the electromagnetic coils. This is equivalent to a power consumption of approximately 26 mW at 4 V_{dc}. In the case for electrothermal actuation, the thermal power consumption plays a more pivotal role in the electrothermal actuator performance compared to the magnitude of the current in electromagnetic actuation. Both electrothermal actuators 1 and 2 are biased serially during the characterization process, while the same is also applied to electrothermal actuators 3 and 4. As observed from figure 7, there is a slight discrepancy between the *I*–*V* curves for the two sets of electrothermal actuators even though the layouts for both sets of actuators are the same. This may be due to the lithography inaccuracy and fabrication process variation. At 3 V_{dc}, the two sets of electrothermal actuators 1 and 2, 3 and 4 have a thermal power consumption of approximately 21 mW and 19 mW respectively.

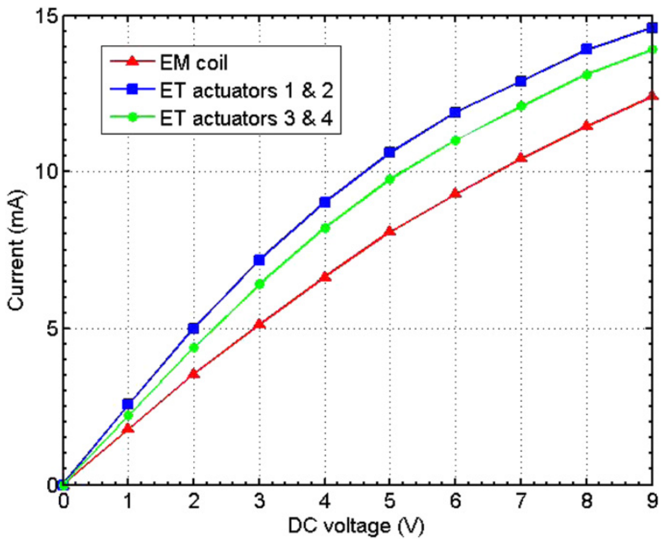

Figure 7. Measured *I*–*V* curves for the EM coils and ET actuators respectively.

Besides the *I*–*V* characteristics of the electromagnetic coils and the electrothermal actuators, several experiments have also been carried out to study both the electrothermal and electromagnetic attenuation in terms of static rotation angle and attenuation response under dc bias.

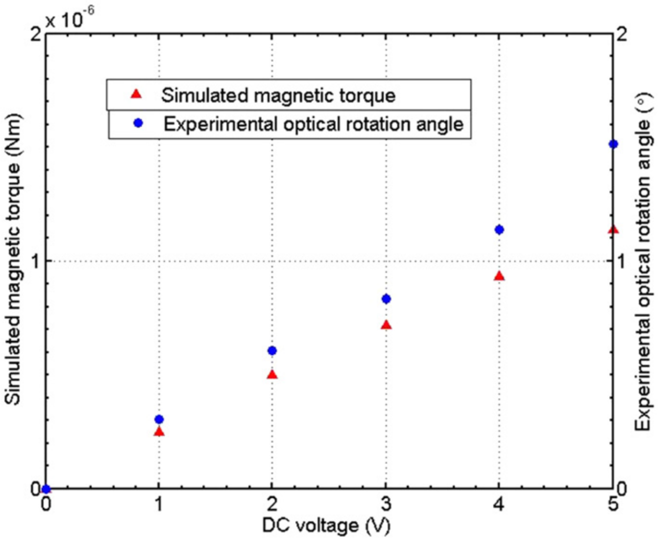

Figure 8. Analytically calculated magnetic torque versus dc driving voltage and experimental optical rotation angle versus dc driving voltage obtained from He/Ne red laser experiment.

4.1. Optomechanical performance for the electromagnetic attenuation scheme

Figure 8 shows both the magnetic torque derived analytically and optical rotation angle obtained experimentally for various dc-driving voltages. The magnetic torque is analytically calculated from (2), with the values of the current input in the electromagnetic coils obtained from the *I–V* curve in figure 7. In the case for the experimental optical rotation angle, it is obtained by shining a red He/Ne laser beam onto the mirror surface and measuring the displacements of the red laser spot on the screen when different dc voltages are applied to the electromagnetic coils. Details of the He/Ne red laser experimental setup can be found in [3–5]. As evident from the curves in figure 8, an increase in dc voltage results in a larger magnetic torque and optical rotation angle. This is expected as an increase in applied voltage will result in a larger current flowing in the electromagnetic coils, causing a larger Lorentz force to be acting on the frame. This causes a larger magnetic torque generated and hence rotates the mirror along the *z*-axis to a greater extent. An experimental optical rotation angle of 1.1° is obtained at 4 V_{dc}.

Figure 9(*a*) shows the displacement of the IR laser spot from its original position ($\delta_{EM,laser}$) corresponding to minimum insertion loss at various dc voltages. Values for the laser spot displacements are derived from the experimental values of the optical rotation angle (θ_{EM}) obtained in figure 8 and substituting these values into equations (3) and (4). From figure 9(*a*), it is observed that the displacement of the laser spot, $\delta_{EM,laser}$, is approximately 21 μm at 4 V_{dc}. The inset shows the front profile of the mirror and the dual-fiber collimator during electromagnetic attenuation. Before electromagnetic actuation when there is no current flowing in the coils, the normal of the mirror surface is perfectly aligned with the IR laser beam, hence coupling all the light from the input fiber to the output fiber, i.e. minimum insertion loss condition. When the mirror rotates due to a dc bias applied to the electromagnetic coils, the IR laser spot is displaced by $\delta_{EM,laser,}$ resulting in attenuation as a portion of the laser beam no longer couples into the output fiber. Based on the VOA characterization setup shown in figure 6, the measured attenuation curves versus dc voltage applied to the electromagnetic coils for different current directions are shown in figure 9(*b*). The experiment is carried out at a fixed laser wavelength of 1550 nm as it is one of the three transmission windows where light attenuation and dispersion in the optical fiber are at the minimum during propagation. Both current directions in the electromagnetic coils yield almost identical attenuation characteristics, achieving a 40 dB dynamic attenuation range at 4 V_{dc} and electrical power consumption of 26 mW. A 40 dB dynamic attenuation range is sufficient with regard to most of the commercial applications. Correlating the experimental data obtained at 4 V_{dc} in figures 9(*a*) and (*b*), it may be interpreted that 40 dB attenuation is achieved when the laser spot is displaced 21 μm away from its original position.

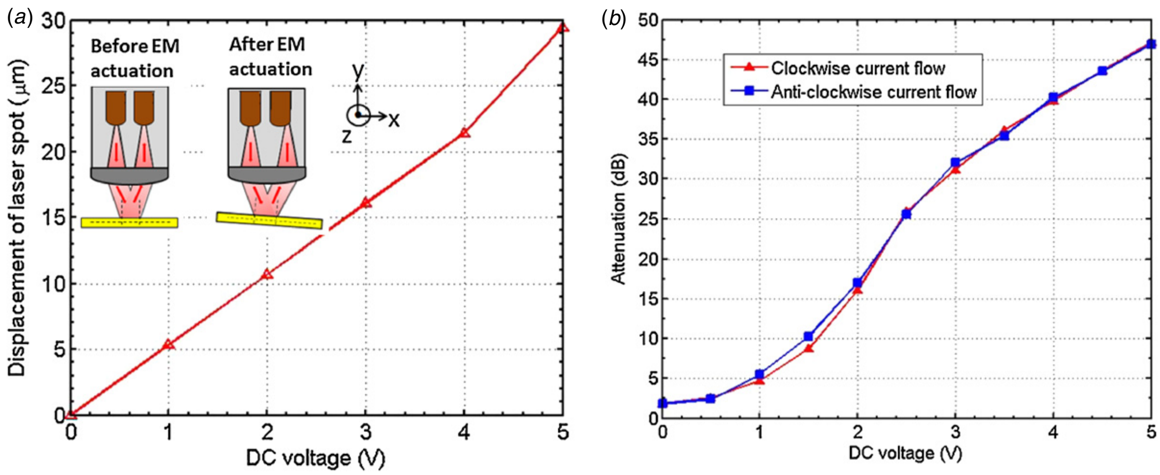

Figure 9. Analytically calculated and experimental data obtained for EM attenuation mechanism. (*a*) Derived IR laser spot displacement versus dc driving voltage applied to the EM coil. The inset shows a schematic diagram of the EM attenuation mechanism, where the laser spot no longer couples perfectly from the input fiber into the output fiber after EM actuation. (*b*) Measured attenuation-bias curves for different current direction in the EM coils.

Table 2. Thermo-mechanical properties of materials used for ET simulation in ANSYS.

Thin film materials	Density (kg m^{-3})	Young's modulus (10^9 Pa)	Poisson ratio	Thermal conductivity (Wm^{-1} K^{-1})	Coefficient of thermal expansion (10^{-6} K^{-1})	Resistivity (10^{-3} Ωm)
Al	2700	65	0.33	237	23.1	2.82×10^{-5}
SiO_2	2200	74	0.17	1.04	0.4	1×10^{19}
Si	2330	162	0.28	150	2.6	100

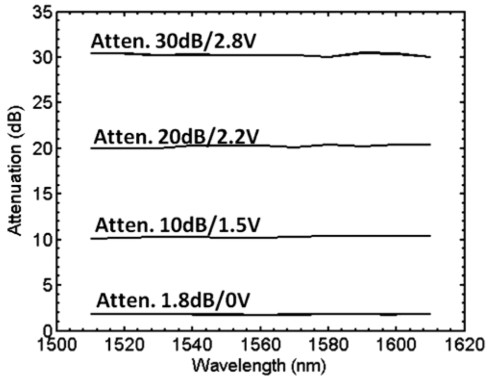

Figure 10. Measured WDL at various attenuation states for EM attenuation.

The wavelength-dependent loss (WDL) from wavelengths within 1510–1610 nm is also measured at various electromagnetic attenuation states and shown in figure 10. The WDL at driving voltages of 0 V_{dc} (1.8 dB), 1.5 V_{dc} (10 dB), 2.2 V_{dc} (20 dB) and 2.8 V_{dc} (30 dB) are less than 0.06 dB, 0.31 dB, 0.39 dB and 0.53 dB respectively. These WDL data measured at the various attenuation states are of the same level with those data already reported in [32–49].

4.2. Optomechanical performance for electrothermal attenuation scheme

In the operation of the MEMS VOA based on electrothermal attenuation scheme, various dc voltages are applied to either one of the two sets of electrothermal actuators 1 and 2 or 3 and 4. Figure 11 compares the mechanical rotation angle (θ) obtained from finite element model (FEM) simulation software ANSYS and the optical rotation angle (2θ) obtained from the He/Ne red laser experiment, with electrothermal actuators 1 and 2 biased at various dc voltages. The thermo-mechanical properties of the different materials used in the ANSYS simulation are summarized in table 2. The mechanical rotation angle derived from simulation matches closely with the optical rotation angle obtained from experiment as the experimental optical rotation angles (2θ) obtained at different dc voltages are almost twice larger than the simulated mechanical rotation angle (θ). The inset in figure 11 shows the simulated *y*-profile of the device obtained from ANSYS when electrothermal actuators 1 and 2 are biased serially at 3 V_{dc}, while an experimental optical rotation angle of 1.1° is obtained at 3 V_{dc}. In addition, parasitic vertical out-of-plane displacement can be noted at the center of the mirror profile obtained from ANSYS simulation. Such out-of-plane displacement may lead to off-center shift of the laser spot. This is due to the limited capability of the four electrothermal actuators to only actively actuate downward, but not upward as it would be needed for pure tilt motion without the off-center shift of the laser spot.

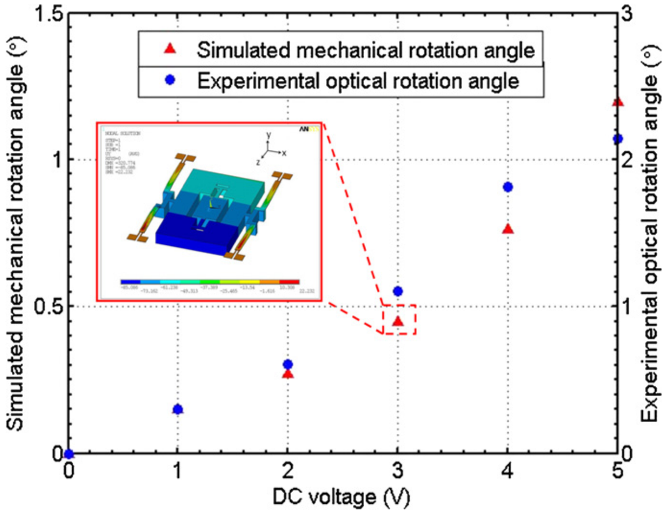

Figure 11. Comparison of the mechanical rotation angle (θ) obtained from simulation software ANSYS and optical rotation angle (2θ) obtained from He/Ne red laser experiment. The inset shows the simulated *y*-profile of the device obtained from ANSYS when ET actuators 1 and 2 are biased serially at 3 V_{dc}.

The displacement of the laser spot for electrothermal attenuation for different dc voltages, which is represented in figure 12(*a*), is also analytically calculated from equation (5) based on the experimental rotation angle derived in figure 11. The inset shows schematic diagrams illustrating the side profile of the mirror and the dual-fiber collimator during electrothermal attenuation. When there is no bias applied to the electrothermal actuators, all the light from the input fiber is coupled to the output fiber, i.e. minimum insertion loss condition. However, when electrothermal actuators 1 and 2 are biased and heated up, they bend downward and actuate the mirror during the process. As a result, the reflected light deviates from the optimized light path corresponding to minimum insertion loss. The coupled reflected light intensity toward the output fiber is reduced, resulting in increased attenuation with increasing dc voltages. As observed from figure 12(*a*), a laser spot displacement of 19 μm is obtained at 3 V_{dc}.

Figure 12(*b*) shows the attenuation curve measured at 1550 nm when various dc voltages are applied to the two sets of electrothermal actuators. Electrothermal actuators 1 and 2 have slightly better attenuation performance compared to electrothermal actuators 3 and 4. This may be due to a greater amount of electrical power being converted to heating effect for electrothermal actuators 1 and 2 compared to 3 and 4 at the same dc voltage, as evident from the *I–V* curves of the

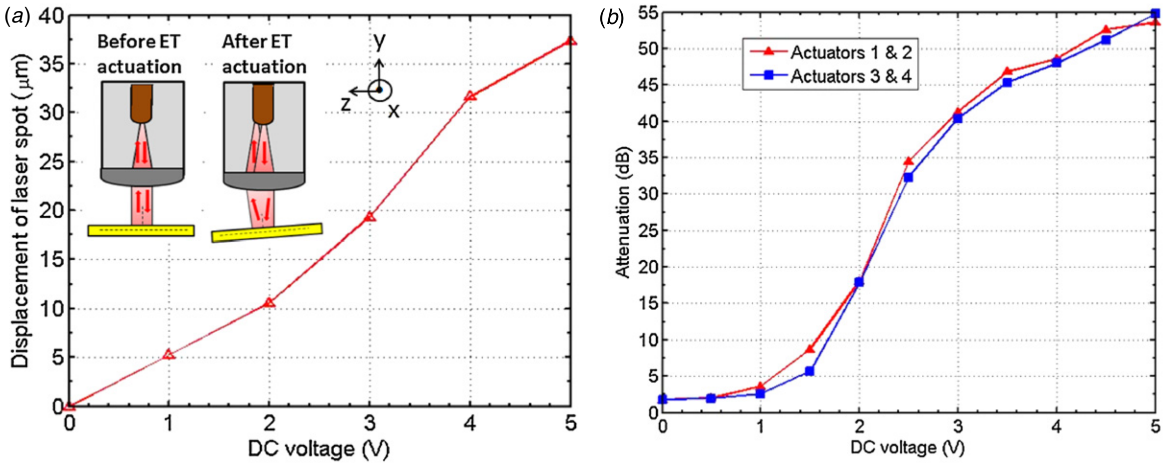

Figure 12. Analytically calculated and experimental data obtained for ET attenuation mechanism. (*a*) Derived IR laser spot displacement versus dc driving voltage applied serially to ET actuators 1 and 2. The inset shows a schematic diagram of the ET attenuation mechanism, where the laser spot no longer couples perfectly from the input fiber into the output fiber after ET actuation. (*b*) Measured attenuation-bias curves for different sets of ET actuators.

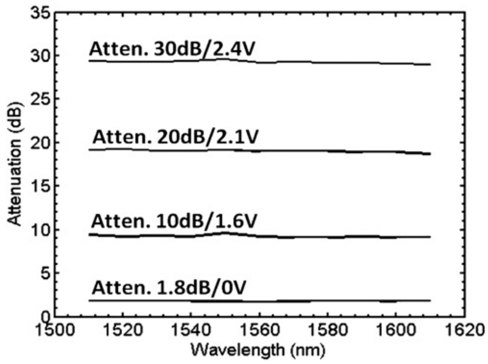

Figure 13. Measured WDL at various attenuation states for ET attenuation.

two sets of electrothermal actuators in figure 7. Both sets of electrothermal actuators, on average, achieve a 40 dB dynamic attenuation range at 3 V_{dc}, and electrical power consumption of 20 mW. Correlating the experimental data obtained at 3 V_{dc} in figures 12(*a*) and (*b*), it may be interpreted that 40 dB attenuation is achieved when the laser spot is displaced 19 μm away from its original position where minimum insertion loss is derived.

The attenuation dependence on wavelength ranging from 1510 nm to 1610 nm is also measured at various electrothermal attenuation states and shown in figure 13. The WDL at driving voltages of 0 V_{dc} (1.8 dB), 1.6 V_{dc} (10 dB), 2.1 V_{dc} (20 dB) and 2.4 V_{dc} (30 dB) are less than 0.06 dB, 0.50 dB, 0.59 dB and 0.63 dB respectively.

Table 3 summarizes and compares the optomechanical performance obtained for both electromagnetic and electrothermal attenuation schemes. To reach 40 dB dynamic attenuation range, voltages of 4 V_{dc} and 3 V_{dc} are needed, with 26 mW and 20 mW of electrical power being consumed by electrothermal and electromagnetic attenuation schemes respectively. Analytical calculations have demonstrated that both attenuation schemes result in almost identical laser spot displacement, while the optical rotation angle (2θ) of the red laser-derived experimentally are the same at 1.1° for both schemes. These results obtained are similar to the data derived in [47] by Isamoto *et al* where optical attenuation of 40 dB, corresponding to the mechanical mirror angle (θ) of 0.3°, was obtained at 5 V_{dc} by their electrostatic microtorsion VOA device. WDL at the 30 dB attenuation state for both attenuation schemes are at similar values to those VOAs already reported in the literature.

In light of the above comparison, we may conclude that the analytical models used to derive the laser spot displacement are valid as both models require close to 20 μm of laser beam displacement in order to reach 40 dB dynamic attenuation range. The validity of the experimental attenuation results obtained are also verified separately through the He/Ne red laser experiment where the optical rotation angle required to reach 40 dB attenuation range in both schemes are the same. In addition, based on the optomechanical performance matrix, electrothermal attenuation scheme is better than electromagnetic attenuation as it consumes less electrical power for the same attenuation state. In terms of driving mechanisms, attenuation scheme based on electrothermal actuation is preferred over that of electromagnetic actuation as the former does not require an external magnetic source, hence offers better scaling viability and compact packaging. Despite the inherent disadvantage of the frequency capability of electrothermal actuation being limited by the heat transfer into and out of the actuator, this is presently not a pressing issue in the operation of MEMS VOA as only dc operations are involved.

4.3. *Optomechanical performance for hybrid attenuation scheme*

In hybrid attenuation scheme, dc voltages are applied simultaneously to the electromagnetic and electrothermal actuators simultaneously. As shown in figure 14, various dc voltage combinations are applied to the two different actuators and an attenuation characteristic topography is

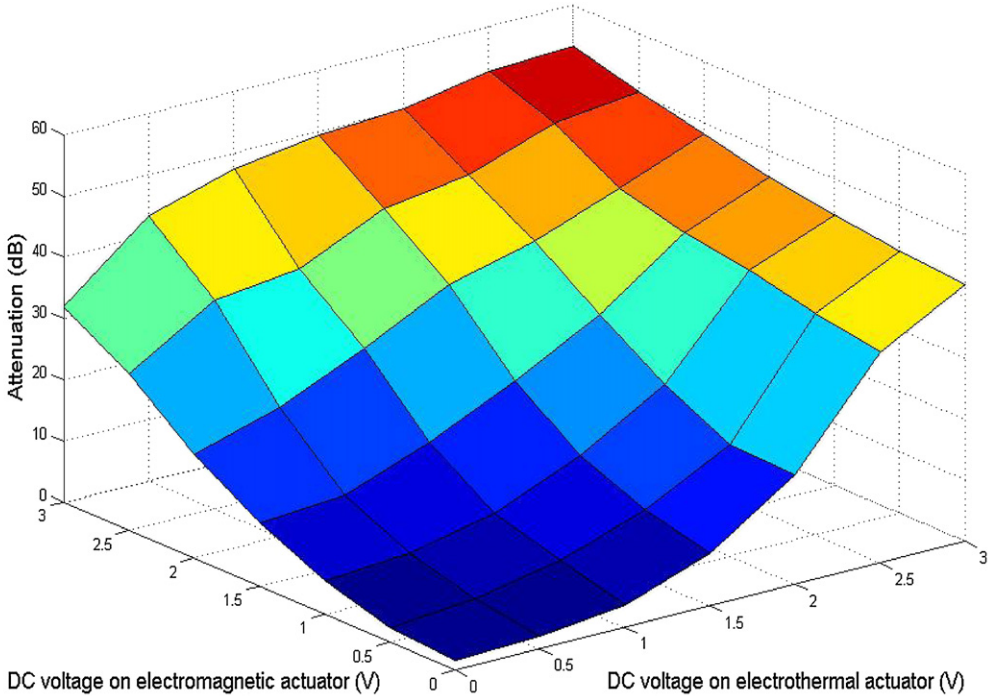

Figure 14. Measured attenuation value as a function of dc driving voltages applied to EM and ET actuators during hybrid actuation.

Table 3. Comparison of the optomechanical performance for EM and ET attenuation.

Attenuation state	40 dB				30 dB
Performance parameters	Voltage (V)	Electrical power consumption (mW)	Displacement of laser spot (μm)	Optical rotation angle (°)	WDL (dB)
Electromagnetic	4	26	21	1.1	0.53
Electrothermal	3	20	19	1.1	0.63

derived. For example, when a bias of 1.5 V_{dc} is applied serially to electrothermal actuators 1 and 2, the attenuation changes from 8.6 dB to 49.4 dB as the voltage applied to the electromagnetic coils increases from 0 V_{dc} to 3 V_{dc}. For the reverse case, i.e. a voltage of 1.5 V_{dc} is applied to the electromagnetic coils, the attenuation changes from 10.3 dB to 45.8 dB as the voltage applied serially to the electrothermal actuators 1 and 2 increases from 0 V_{dc} to 3 V_{dc}. Hence from the attenuation topography, various voltage combinations can be made to the electromagnetic and electrothermal actuators so as to obtain a 40 dB dynamic attenuation range. For example, when 2 V_{dc} are applied to both the electromagnetic and electrothermal actuators simultaneously, an attenuation of approximately 40 dB can be obtained. This is equivalent to a total electrical power consumption of 17 mW, which is 3 mW lower than that achieved by electrothermal attenuation scheme at 3 V_{dc}. As such, with the hybrid attenuation scheme, lower electrical power consumption and an additional degree of freedom in attenuation control can be attained. More specifically, any deviation of attenuation–dc bias characteristics among the various VOA devices due to the fabrication process and assembly steps can be compensated by changing the voltage combinations to the electromagnetic and electrothermal actuators. By adopting electrothermal actuation as the primary attenuation scheme and electromagnetic attenuation for compensating any small deviations among the various VOA devices, smaller magnets of weaker magnetic field strength may be used, hence allowing room for miniature packaging.

5. Concluding remarks

A novel MEMS mirror based on hybrid actuation mechanisms is proposed and verified for variable optical attenuation in a 3D free space configuration. Both electromagnetic and electrothermal actuations have been integrated in the same device for optical attenuation purposes. This makes our design essentially different from most of the shutter type, planar reflective and 3D reflective VOAs that have already been reported in the literature where only one actuation mechanism is used to drive the shutter or mirror. Dynamic attenuation ranges of 40 dB have been achieved at 4 V_{dc}, 26 mW and 3 $V_{dc,}$ 20 mW by electromagnetic and electrothermal attenuation schemes respectively. Wavelength-dependent loss has also been demonstrated to be less than 0.6 dB at all attenuation states for both attenuation schemes. Electrothermal attenuation scheme has been concluded to perform better than electromagnetic attenuation as it consumes less electrical power for the same attenuation state and it removes the need for an external magnetic source. Hybrid attenuation scheme has also been demonstrated successfully, allowing our device to consume even lesser electrical power and attain an additional degree of freedom in attenuation control.

Optimization in terms of reduction of driving voltage is the next step to further improve the performance of our MEMS VOA devices. The thickness of the bulk silicon beneath the mirror plate and the outer frame may be further reduced so as to decrease the mass inertia and operating voltage of the device. More electromagnetic coils may be fabricated to increase the magnetic torque contribution at a lower voltage. Last but not the least, the use of CMOS-compatible processes and material such as aluminum and silicon oxide for electrothermal and electromagnetic actuation allow our design to be fully transferable to various foundry orientated CMOS–MEMS fabrication platforms such as the TSMC standard 0.35 μm 2P4M process. This allows for lower fabrication cost and monolithic integration with transistor circuits that enable a hybrid-actuated MEMS VOA with electronic feedback to be developed.

Acknowledgments

The authors would like to acknowledge the financial contributions from University Research Fund under grant no R-263-000-692-112 at the National University of Singapore, Singapore and the PhD scholarship grant received from GlobalFoundries, Singapore.

References

[1] Kobayashi T, Maeda R, Itoh T and Sawada R 2007 Smart optical microscanner with piezoelectric resonator, sensor, and tuner using Pb(Zr,Ti)O_3 thin film *Appl. Phys. Lett.* **90** 183514

[2] Tang T-L, Hsu C-P, Chen W-C and Fang W 2010 Design and implementation of a torque-enhancement 2-axis magnetostatic SOI optical scanner *J. Micromech. Microeng.* **20** 025020

[3] Koh K H, Kobayashi T, Hsiao F-L and Lee C 2010 Characterization of piezoelectric PZT beam actuators for driving 2D scanning micromirrors *Sensors Actuators* A **162** 336–47

[4] Koh K H, Kobayashi T, Xie J, Yu A and Lee C 2011 Novel piezoelectric actuation mechanism for a gimbal-less mirror in 2D raster scanning applications *J. Micromech. Microeng.* **21** 075001

[5] Koh K H, Kobayashi T and Lee C 2011 A 2-D MEMS scanning mirror based on dynamic mixed mode excitation of a piezoelectric PZT thin film S-shaped actuator *Opt. Exp.* **19** 13812–24

[6] Wang Y, Raj M, McGuff H S, Bhave G, Yang B, Shen T and Zhang X 2012 Portable oral cancer detection using a miniature confocal imaging probe with a large field of view *J. Micromech. Microeng.* **22** 065001

[7] Pan Y, Xie H and Fedder G K 2001 Endoscopic optical coherence tomography based on a microelectromechanical mirror *Opt. Lett.* **26** 1966–8

[8] Wolffenbuttel R F 2005 MEMS-based optical mini- and microspectrometers for the visible and infrared spectral range *J. Micromech. Microeng.* **15** S145-52

[9] Noell W, Clerc P A, Dellmann L, Guldimann B, Herzig H P, Manzardo O, Marxer C R, Weible K J, Dandliker R and de Rooij N 2002 Applications of SOI-based optical MEMS *IEEE J. Sel. Top. Quantum Electron.* **8** 148–54

[10] Walker J A 2000 The future of MEMS in telecommunications networks *J. Micromech. Microeng.* **10** R1–7

[11] Lin L Y and Goldstein E L 2002 Opportunities and challenges for MEMS in lightwave communications *IEEE J. Sel. Top. Quantum Electron.* **8** 163–72

[12] Wu M C, Solgaard O and Ford J E 2006 Optical MEMS for lightwave communication *IEEE/OSA J. Lightw. Technol.* **24** 4433–54

[13] Lee C and Yeh J A 2008 Development and evolution of MOEMS technology in variable optical attenuators *J. Micro/Nanolith. MEMS MOEMS* **7** 021003

[14] Toshiyoshi H and Fujita H 1996 Electrostatic micro torsion mirrors for an optical switch matrix *IEEE/ASME J. Microelectromech. Syst.* **5** 231–7

[15] Lee C and Wu C-Y 2005 Study of electrothermal V-beam actuators and latched mechanism for optical switch *J. Micromech. Microeng.* **15** 11

[16] Marxer C, Thio C, Gretillat M A, de Rooij N F, Battig R, Anthamatten O, Valk B and Vogel P 1997 Vertical mirrors fabricated by deep reactive ion etching for fiber-optic switching applications *IEEE/ASME J. Microelectromech. Syst.* **6** 277–85

[17] Liu A Q and Zhang X M 2007 A review of MEMS external-cavity tunable lasers *J. Micromech. Microeng.* **17** R1–13

[18] Bell D J, Lu T J, Fleck N A and Spearing S M 2005 MEMS actuators and sensors: observations on their performance and selection for purpose *J. Micromech. Microeng.* **15** S153

[19] Trolier-McKinstry S and Muralt P 2004 Thin film piezoelectrics for MEMS *J. Electroceram.* **12** 7–17

[20] Muralt P, Polcawich R G and Trolier-McKinstry S 2009 Piezoelectric thin films for sensors, actuators, and energy harvesting *MRS Bull.* **34** 658–64

[21] Isarakorn D, Sambri A, Janphuang P, Briand D, Gariglio S, Triscone J M, Guy F, Reiner J W, Ahn C H and de Rooij N F 2010 Epitaxial piezoelectric MEMS on silicon *J. Micromech. Microeng.* **20** 055008

[22] Reinke J, Fedder G K and Mukherjee T 2010 CMOS-MEMS variable capacitors using electrothermal actuation *IEEE/ASME J. Microelectromech. Syst.* **19** 1105–15

[23] Chen W C, Fang W and Li S S 2012 High-Q integrated CMOS-MEMS resonators with deep-submicrometer gaps and quasi-linear frequency tuning *IEEE/ASME J. Microelectromech. Syst.* **21** 688–701

[24] Lange D, Hagleitner C, Herzog C, Brand O and Baltes H 2003 Electromagnetic actuation and MOS-transistor sensing for CMOS-integrated micromechanical resonators *Sensors Actuators* A **103** 150–5

[25] Yeh J L A, Jiang H and Tien N C 1999 Integrated polysilicon and DRIE bulk silicon micromachining for an electrostatic torsional actuator *IEEE/ASME J. Microelectromech. Syst.* **8** 456–65

[26] Dooyoung H, Patterson P R, Nguyen H D, Toshiyoshi H and Wu M C 2004 Theory and experiments of angular vertical comb-drive actuators for scanning micromirrors *IEEE J. Sel. Top. Quantum Electron.* **10** 505–13

[27] Que L, Park J S and Gianchandani Y B 2001 Bent-beam electrothermal actuators—part I: single beam and cascaded devices *IEEE/ASME J. Microelectromech. Syst.* **10** 247–54

[28] Todd S T and Xie H 2008 An Electrothermomechanical lumped element model of an electrothermal bimorph actuator *IEEE/ASME J. Microelectromech. Syst.* **17** 213–25

[29] Kwan A M H *et al* 2012 Improved designs for an electrothermal in-plane microactuator *IEEE/ASME J. Microelectromech. Syst.* **21** 586–95

[30] Yang H-A, Tang T-L, Lee S T and Fang W 2007 A novel coilless scanning mirror using eddy current lorentz force and magnetostatic force *IEEE/ASME J. Microelectromech. Syst.* **16** 511–20

[31] Fan K-C, Lin W-L, Chiang L-H, Chen S-H, Chung T-T and Yang Y-J 2009 A 2 × 2 Mechanical optical switch with a thin MEMS Mirror *IEEE/OSA J. Light.Technol.* **27** 1155–61
[32] Giles C R, Aksyuk V, Barber B, Ruel R, Stulz L and Bishop D 1999 A silicon MEMS optical switch attenuator and its use in lightwave subsystems *IEEE J. Sel. Top. Quantum Electron.* **5** 18–25
[33] Marxer C, Griss P and de Rooij N F 1999 A variable optical attenuator based on silicon micromechanics *IEEE Photonics Technol. Lett.* **11** 233–5
[34] Liu A Q, Zhang X M, Lu C, Wang F, Lu C and Liu Z S 2003 Optical and mechanical models for a variable optical attenuator using a micromirror drawbridge *J. Micromech. Microeng.* **13** 400–11
[35] Lee C, Lin Y-S, Lai Y-J, Tasi M H, Chen C and Wu C-Y 2004 3-V driven pop-up micromirror for reflecting light toward out-of-plane direction for VOA applications *IEEE Photonics Technol. Lett.* **16** 1044–6
[36] Zhang X M, Zhao Q W, Liu A Q, Zhang, Lau J H and Kam C H 2008 Asymmetric tuning schemes of MEMS dual-shutter VOA *IEEE/OSA J. Light. Technol.* **26** 569–79
[37] Syms R R A, Zou H, Stagg J and Veladi H 2004 Sliding-blade MEMS iris and variable optical attenuator *J. Micromech. Microeng.* **14** 1700–10
[38] Hung S H, Hsieh H T and Su G D J 2008 An electro-magnetic micromachined actuator monolithically integrated with a vertical shutter for variable optical attenuation *J. Micromech. Microeng.* **18** 075003
[39] Zhang X M, Liu A Q, Lu C and Tang D Y 2002 MEMS variable optical attenuator using low driving voltage for DWDM systems *Electron. Lett.* **38** 382–3
[40] Cai H, Zhang X M, Lu C, Liu A Q and Khoo E H 2005 Linear MEMS variable optical attenuator using reflective elliptical mirror *IEEE Photonics Technol. Lett.* **17** 402–4
[41] Hou M T-K, Huang J-Y, Jiang S-S and Yeh J A 2008 In-plane rotary comb-drive actuator for a variable optical attenuator *J. Micro/Nanolith. MEMS MOEMS* **7** 043015
[42] Yeh J A, Jiang S-S and Lee C 2006 MOEMS variable optical attenuators using rotary comb drive actuators *IEEE Photon. Technol. Lett.* **18** 1170–2
[43] Chen C, Lee C and Yeh J A 2004 Retro-reflection type MOEMS VOA *IEEE Photonics Technol. Lett.* **16** 2290–2
[44] Lee C 2007 A MEMS VOA using electrothermal actuators *IEEE/OSA J. Light. Technol.* **25** 490–8
[45] Lim T-S, Ji C-H, Oh C-H, Kwon H, Yee Y and Bu J U 2004 Electrostatic MEMS variable optical attenuator with rotating folded micromirror *IEEE J. Sel. Top. Quantum Electron.* **10** 558–62
[46] Zhang X M, Liu A Q, Cai H, Yu A B and Lu C 2007 Retro-axial VOA using parabolic mirror pair *IEEE Photonics Technol. Lett.* **19** 692–4
[47] Isamoto K, Kato K, Morosawa A, Changho C, Fujita H and Toshiyoshi H 2004 A 5-V operated MEMS variable optical attenuator by SOI bulk micromachining *IEEE J. Sel. Top. Quantum Electron.* **10** 570–8
[48] Lee C, Hsiao F-L, Kobayashi T, Koh K H, Ramana P V, Xiang W, Yang B, Tan C W and Pinjala D 2009 A 1–V operated MEMS variable optical attenuator using piezoelectric PZT Thin-Film actuators *IEEE J. Sel. Top. Quantum Electron.* **15** 1529–36
[49] Koh K H, Lee C and Kobayashi T 2010 A piezoelectric-driven three-dimensional MEMS VOA using attenuation mechanism with combination of rotational and translational effects *IEEE/ASME J. Microelectromech. Syst.* **19** 1370–9